One-pot synthesis of high-capacity silicon-lithium anodes *via* on-copper growth of a semi-conducting, porous polymer

Jieyang Huang[1], Andréa Martin[1], Anna Urbanski[2], Ranjit Kulkarni[1], Patrick Amsalem[3], Moritz Exner[1], Johannes Müller[3], David Burmeister[1], Norbert Koch[3,4], Nicola Pinna[1], Petra Uhlmann[2], Michael J. Bojdys[,1,5]*

[1] Institut für Chemie and IRIS Adlershof, Humboldt-Universität zu Berlin, Brook-Taylor-Str. 2, 12489 Berlin, Germany.

[2] Leibniz-Institut für Polymerforschung Dresden (IPF) e. V., Institut für Physikalische Chemie and Physik der Polymere, 01069 Dresden, Germany.

[3] Institut für Physik and IRIS Adlershof, Humboldt-Universität zu Berlin, Brook-Taylor-Str. 2, 12489 Berlin, Germany.

[4] Helmholtz-Zentrum Berlin GmbH, Albert-Einstein-Str. 15, 12489 Berlin, Germany

[5] Department of Chemistry, King's College London, Britannia House Guy's Campus, 7 Trinity Street, London, SE1 1DB, UK.

KEYWORDS: Graphdiyne, Glaser-coupling, Li-ion battery, Silicon anode, One-pot.

ABSTRACT

Silicon-based anodes with lithium ions as charge carriers have the highest predicted charge density of 3579 mA h g^{-1} (for $Li_{15}Si_4$) while being comparatively safe. Contemporary electrodes do not achieve these theoretical values largely because production paradigms remained unchanged since their inception and rely on the mixing of weakly coordinated, multiple components. In this paper, we present the one-pot synthesis of high-performance anodes that reach the theoretical capacity of the fully lithiated state of silicon. Here, a semi-conductive triazine-based graphdiyne polymer network is grown around silicon nanoparticles directly on the current collector, a copper sheet. The current collector (Cu) acts as the catalyst for the formation of a semi-conductive triazine-based graphdiyne polymer network that grows around the inorganic, active material (Si). In comparison to established electrode assemblies, this process (i) omits any steps related to curing, drying, and annealing, (ii) does away with binders and conductivity-enhancing additives that decrease volumetric and gravimetric capacity, and (iii) cancels out the detrimental effects on performance, chemical and physical stability of conventional, three-component anodes (Si, binder, carbon black). This is because, the porous, semi-conducting organic framework (i) adheres to the current collector on which it grows *via* cooperative van der Waals interactions, (ii) acts effectively as conductor for electrical charges and binder of silicon nanoparticles *via* conjugated, covalent bonds, and (iii) enables selective transport of mass and charge-carriers (electrolyte and Li-ions) through pores of defined size. As a result, the anode shows extraordinarily high capacity at the theoretical limit of fully lithiated silicon, excellent performances in terms of cycling (exceeding 70% capacity retention after 100 cycles), and high mechanical and thermal stability. Finally, we combine our anodes in proof-of-concept full battery assemblies using a number of conventional cathodes (NCM811). These high-performance anodes pave the way for use in flexible, wearable electronics and in environmentally demanding applications.

INTRODUCTION

Cheap, high-performance, and safe energy storage solutions are needed to address the increasing demand for portable electronics and the transition to electric mobility. Lithium-ion batteries have replaced conventional secondary battery technology (like nickel-cadmium and nickel-metal hydride batteries) due to their high energy densities, high operating voltages, and stable capacity retention during open-circuit rest.[1] Lithium metal anodes were quickly replaced by lithium-intercalated graphitic materials in order to avoid the formation of dendrites that resulted in short circuiting of the two electrodes. However, while lithium-graphite intercalates are safer and more stable they have only a tenth of the energy density of metallic lithium.[2] Silicon is a good active material for Li-ion anodes because it has a superior theoretical capacity of 3579 mA h g^{-1} (or 8340 mA h cm^{-3}) for $Li_{15}Si_4$, and – unlike some transition metals – it is not toxic and abundant. Moreover, its alloying reaction with lithium triggered at 0.3 V vs. Li/Li^+, prevents the formation of metallic lithium around the anode during discharging – a detrimental process observed for Li-graphite batteries known as "lithium plating" – and allows the use of Si-Li electrodes under harsher conditions.[3] The large number of lithium atoms that silicon can store, however, induces large volume changes during charge/discharge cycles (>300%).[3] The mechanical stress induced by these drastic volume changes leads to the pulverization of the silicon active material, loss of contact of the electrode film with the current collector, and loss of overall mechanical integrity of the whole electrode. Repeated cycles of expansion and contraction of silicon expose pristine silicon surfaces and induce the reformation of solid electrolyte interfaces (SEI). This process contributes to the gradual consumption of lithium and electrolyte, and it limits the diffusion of charge carriers through the expanding SEI.[3-7] It is difficult to counter these detrimental mechanical and chemical changes to silicon-based electrodes because conventional methods of electrode assembly rely on the mixing of multiple components that are held together by weak, dispersive forces.

In laboratory settings, some strategies were developed to address the inherent flaws of these multi-component assemblies. For example, shaping silicon into hierarchical, nano-sized, or porous structures buffers some of its dramatic volume expansion during lithiation.[7] On the downside, nanostructured silicon is susceptible to restructuring during battery operation, and its larger specific surface promotes reactions with the electrolyte to form more of electrochemically inactive SEI. In other approaches silicon particles are encapsulated in a carboneous matrix,[8] or they are coated with metal oxides.[9] However, encapsulation of silicon requires supplementary components that do not meaningfully contribute to the volumetric capacity of the electrode and might necessitate the addition of agents that enhance electric conductivity. Such modifications of the active material prior to electrode assembly have proven too time consuming, low yielding and expensive and, hence, none of these methods have found their way into commercial processes to date.

In this work, we present a departure from the current "blend-and-bake" paradigm of electrode manufacture. In a one-pot process, we embed silicon nanoparticles (Si NPs) in a covalently-linked, porous, semi-conducting polymer matrix whose growth is initiated and templated by the current collector (Cu) itself. The covalent bonds of the organic matrix contribute to a superior mechanical and chemical resistance of our electrode films. The overall π-conjugated backbone of the triazine-based graphdiyne (TzG) polymer enables the transport of electrons from the active material to the current collector. Since the polymerization is promoted by the reactive metal surface of the current collector, the resulting polymer/silicon composite (TzG/Si) adheres strongly to it.[10] In summary, the covalent polymer matrix acts at the same time as (i) a strong binder, as (ii) an electrical conductor, and as (iii) a semi-permeable membrane that enables transport of ions and electrolyte but prevents the migration of homogeneously dispersed silicon nanoparticles even under harsh conditions. This facile method yields silicon-based anodes (TzG/Si@Cu) of superior performance that suffer little

mechanical and electrochemical deterioration from the inherent volume expansion of silicon during lithiation-delithiation cycles and that drastically limit the detrimental loss of lithium and electrolyte at the solid electrolyte interface.

Electrodes of TzG/Si@Cu are prepared by dissolving the organic monomer 2,4,6-tris(4-ethynylphenyl)-1,3,5-triazine and dispersing Si NPs in pyridine in a 25%:75% weight ratio, respectively. The reaction mixture is then transferred onto a copper foil (Figure 1a; Supplementary Information Section 1, Scheme S1 and S2). Residual Cu(II) and Cu(I) species on the untreated copper surface initiate the polymerization *via* a Glaser-type oxidative coupling reaction.[11-13] The polymerization is driven to completion and the pyridine is gradually removed by evaporation at 60 °C over three days.[10] ^{13}C cross-polarization–magic-angle-spinning (CP–MAS) solid-state NMR (Figure 1b) shows the characteristic signals of a triazine-based graphdiyne polymer;[10] the triazine carbon at ~170 ppm and the diyne-bridges at 75-85 ppm. An additional signal seen at ~30 ppm is attributed to O_2SiMe_2 surface groups originating from the preparation of these commercially available Si NPs. This is corroborated by ^{29}Si single-pulse-magic-angle-spinning (SP-MAS) solid-state NMR (Figure S1) and Fourier transform infrared (FT-IR) spectra (Figure S2).[14-16] The Raman spectrum of TzG/Si@Cu (Figure 1c) shows stretching bands of diyne C≡C at 2209 cm^{-1}, of triazine C=N at 1411 cm^{-1}, of phenyl C=C at 1604 cm^{-1}, and of crystalline Si-Si bonds at 518 cm^{-1}.[10,17,18]

X-ray photoelectron spectroscopy (XPS) performed on c-axis oriented layers of TzG/Si@Cu show all expected carbon environments in the C 1s region that are observed for the neat TzG polymer (Figure S3a).[10] In addition, Si 2p spectra show the presence of surface silicon oxide, SiO_x (~34%) and neat silicon (66%) (Figure S3b), compared to as-received Si NPs that contain 21% of SiO_x and 79% of Si(0) environments (Figure S3d).[19-22] In summary, spectroscopic analysis confirms the formation of a covalent, conjugated, triazine-based polymer network around chemically unchanged Si NPs.

For comparison, we have prepared three different types of electrode systems *via* the same one-pot method described above but with varying compositions to carefully test the effects of individual components: (i) growing a film of TzG on Cu, we obtain TzG@Cu, (ii) growing TzG in the presence of Si NPs we get TzG/Si@Cu, and (iii) TzG/Si/CB@Cu is produced by growing TzG around Si NPs and a conventional, conductive additive, carbon black (CB) (Supplementary Information Section S1.6).

Scanning electron microscopy (SEM) images reveal the morphology of pristine TzG/Si@Cu electrodes. The material grown on the copper support adopts a porous, sponge-like, and homogeneous morphology as seen top-down (Figure 1e) and from cross-sections of the electrode film (Figure 1f). Cross-sectional SEM imaging at lower magnifications shows films of TzG/Si with a thickness of ~25 µm that adhere well to the Cu substrate with no apparent gaps (Figure S4). More detailed transmission electron microscopy (TEM) energy-filtered mapping on TzG/Si films shows a homogenous distribution of carbon and silicon on the nano-scale (Figure 1g). On the nanoscale, the electrode film consists of Si NPs homogenously embedded in an organic polymer matrix of TzG. Residual Cu nanoparticles can be seen withing the polymer matrix that stem from the TzG polymerization process (Figure 1h; a comparison of TEM images of TzG@Cu and of pristine Si NPs can be found in Figure S5).[10] Overall, individual Si NPs are enclosed by the conjugated, polymer and held cooperatively as a film on the current collector.

We have shown previously that neat, unmodified triazine-based graphdiyene polymers are narrow-band gap semiconductors ($E_{g,elec}$ = 1.84 eV and conductivity of 1.2 µS cm^{-1}) with moderate porosities (N_2 BET surface area of 124 m^2 g^{-1} at 77 K).[10,23] Hence, the composite TzG/Si on Cu foil (TzG/Si@Cu) has a promising combination of chemical, electrical, and structural features for electrochemical storage.

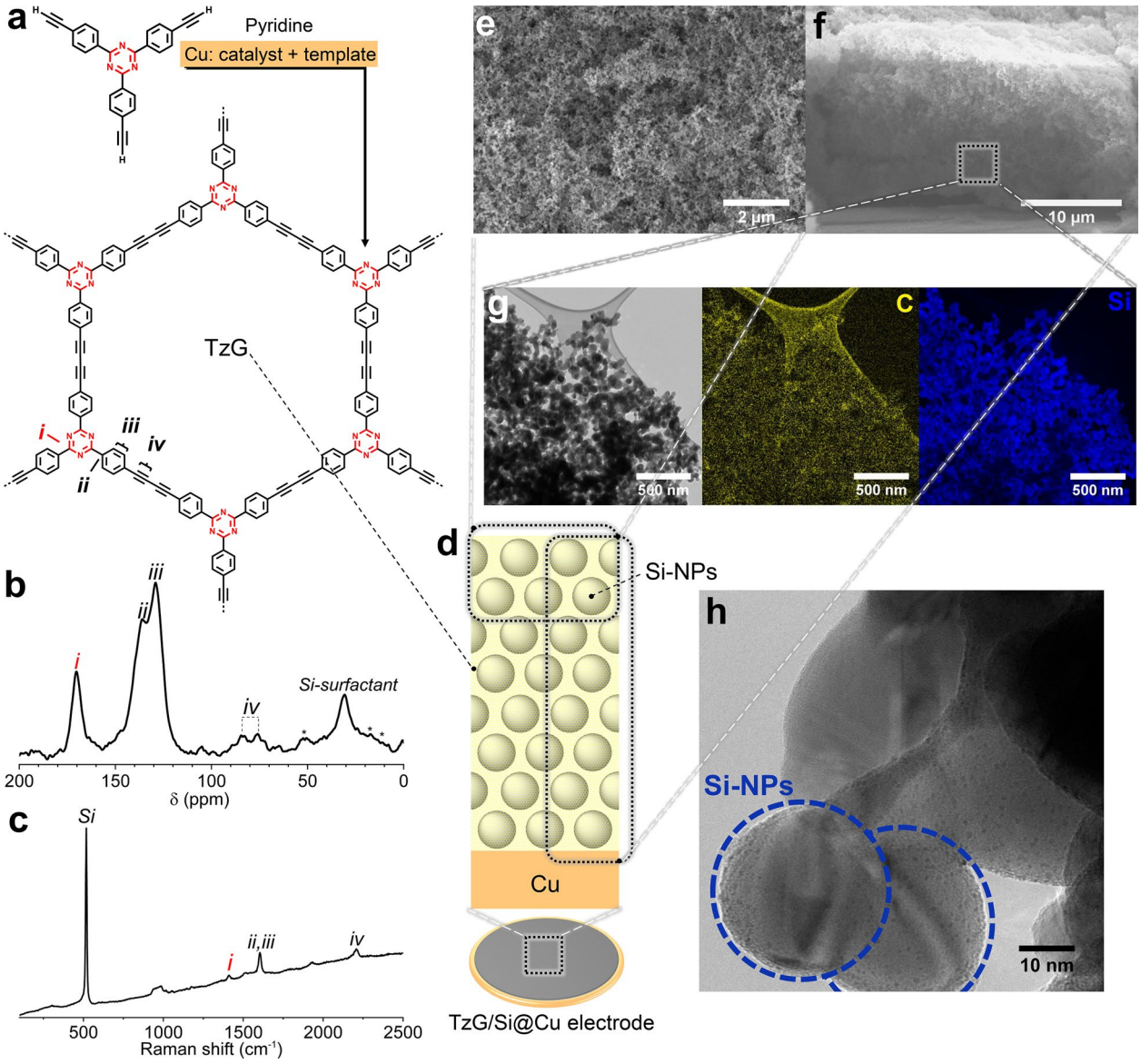

Figure 1. Micro- and macroscopic characterization of the chemical make-up of TzG/Si@Cu (TzG/Si = 25/75 wt%) electrodes prepared following **method 1**. **a**, Synthetic pathway for the triazine-based graphdiyene (TzG) polymer. Spectroscopic characterization showing the corresponding **b**, ^{13}C cross-polarization–magic-angle-spinning (CP–MAS) solid-state NMR spectrum of the TzG/Si polymer composite, and **c**, the Raman spectrum with fluorescence background collected with a 532 nm laser. **d**, Schematic of the TzG/Si@Cu electrode. Scanning electron microscopy (SEM) images showing **e**, the top-view surface morphology and **f**, the cross section morphology of TzG/Si@Cu films. **g**, Low-resolution transmission electron microscopy (TEM) images and energy-filtered mapping images showing the homogenous

distribution of carbon and silicon environments, and **h**, high-resolution TEM images showing Si NPs fully enclosed by TzG polymer.

In the following (Supplementary Information Section S2.1), we discuss the electric and electrochemical performance of TzG-based electrodes and the effects of the TzG polymer on the formation of the SEI. For the three electrode systems TzG/Si@Cu, TzG/Si/CB@Cu, and TzG@Cu (i) we compared the bulk conductivities of the unlithiated, "as-synthesized" electrodes (Figure S6), (ii) we recorded cyclic voltammetry (CV) curves (Figure S7), and (iii) we performed ex-situ XPS measurements probing the electrode surfaces to a depth of approx. 10 nm after a number of de-/lithiation cycles (Figure 2a; Figure S8, S9, S10 and S13; Table S1; details of the XPS spectra fitting method are described in Supplementary Information section S1.11). During the first lithiation of the TzG/Si@Cu electrode, the resulting composition of the film present a content with up to 43.9 mol% of cumulative Li, F. and P elements (Table 1). Furthermore, after the first cycle of lithiation and delithiation, we observe that the initial Si 2p signal of the pristine electrode decreases dramatically in intensity from 40.8 mol% to value close to zero (Table 1). The fitting of C 1s, F 1s and Li 1s spectra (Figure S10) indicate the formation of the SEI during the first lithiation, resulting in the variations of surface elemental concentration mentioned above. Note though that even after the 100th delithiation event, we detect a signal of Si(0) in the Si 2p region (Figure 2a, iv, Table 1). This finding suggests that SEI formation is completed at an early stage, and that SEI thickness does not increase dramatically throughout cycling.[24,25] XPS data from the Si 2p region of TzG/Si@Cu electrodes cycled at C/8 (Figure 2a) shows the emergence of new Si 2p peaks corresponding to Li_xSi, SiO_xF_y, and Li_xSiO_y after the first lithiation event.[19-22] The presence of SiO_xF_y results from the non-faradic reaction between the remaining $LiPF_6$ and the SiO_x on the surface of the Si NPs, during the opening the cell for ex-situ measurement.[19] The environments of Li_xS and Li_xSiO_y originate from the electrochemical alloying reaction of silicon and SiO_x

with the lithium ions in the electrolyte, as further corroborated by emerging signals in the F 1s and Li 1s regions (Figure S10b and S10c).[20,22] Pristine and delithiated samples of TzG/Si@Cu all show peaks corresponding to Si(0) and SiO_x indicating a fully reversible de-/lithiation process.

Ex-situ TEM and SEM imaging of TzG/Si@Cu electrodes at different cycling stages (Figure 2b and c) reveal that prior to cycling, the TzG polymer acts as a binder that joins Si NPs into a porous TzG/Si composite (i). After the first lithiation event, individual particles of increased size can be discerned that correspond to lithiated and volumetrically expanded domains of Li_xSi all embedded in a fabric of polymer and SEI (ii). After the first delithiation, the size of the spherical Si domains decreases (iii), and after the 100^{th} delithiation, all that can be said is that the TzG/Si composite shows no discernible large cracks or deformations (iv) (Figure S11 and S12).

A comprehensive discussion of these findings is presented in Supplementary Information section S2.2. For now, we conclude that: (i) the alloying reaction between lithium and Si NPs takes place unhindered, hence, the TzG polymer matrix allows lithium to diffuse, (ii) the conductivity enhancing additive in TzG/Si/CB@Cu has no positive effect on the performance of TzG-based electrodes, hence, the initial, modest conductivity of undoped TzG is no impediment for its use in electrodes; and (iii) the TzG polymer does not participate in the detrimental depletion of lithium or electrolyte on its own, and SEI formation occurs exclusively in the presence of Si NPs. It is particularly surprising that TzG-based electrodes perform as well as they do, given their low conductivity in the pristine, unlithiated state. While an in-depth study of the electric conductivity of lithiated TzG/Si@Cu is out of the scope of this work, XPS results for TzG@Cu suggest that the first lithiation cycle leads to n-doping of the TzG polymer by N 1s signal shifting to higher binding energy (Figure S8),[26-28] analogous to lithiated

graphite,[29,30] and, hence, to an increase of its conductivity above and beyond the effect achieved by the conducting additive in TzG/Si/CB@Cu.

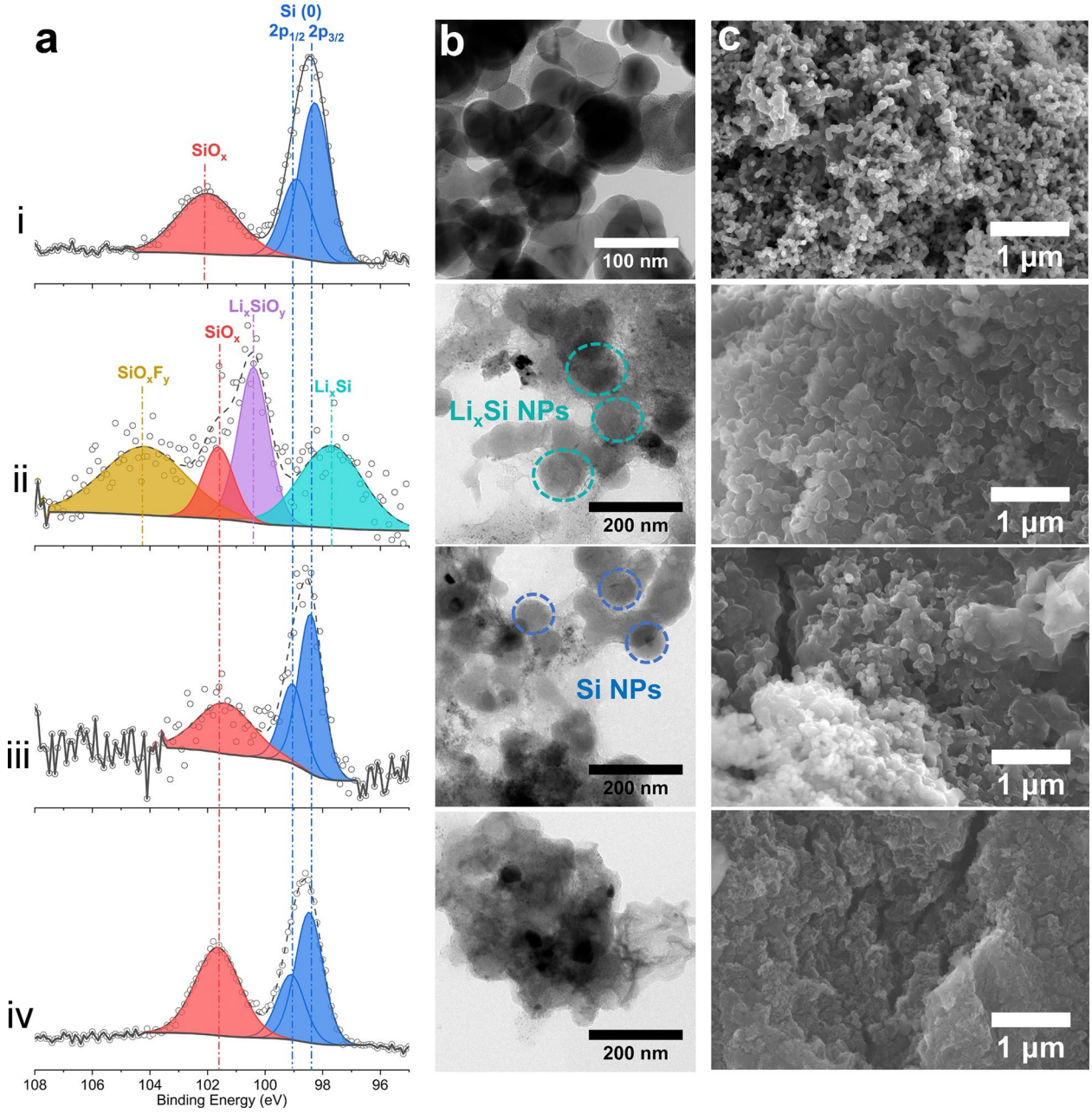

Figure 2. Characterization of TzG/Si@Cu electrodes prepared following **method 1** using **a**, X-ray photoelectron spectroscopy (XPS) data from the Si 2p region, **b**, transmission electron microscopy (TEM), and **c**, scanning electron microscopy (SEM). Data is presented for TzG/Si@Cu electrodes in the pristine state (i), after the first lithiation (ii), after the first

delithiation (iii) and after the 100th delithiation (iv). Cycling was performed at a constant current of 0.32 mA cm^{-2} (*i.e.* C/8 for the capacity of Si, within 0.01-1.2 V vs. Li/Li^{+}).

We subjected the TzG/Si@Cu electrode prepared following **method 1** to de-/lithiation cycling at C/8 in a half-cell set-up recording specific capacity (Figure 3). In the first lithiation cycle, we observe the formation of the SEI at a comparatively low CE value of ~70%, meaning that the surface of Si NPs is readily accessible for lithium and for the electrolyte *via* the pore channels of the TzG polymer. Similar Coulombic efficiencies have been reported for nanosized silicon particles with a large external surface area. Microsized silicon particles with a smaller ratio of exposed surfaces show higher initial CE values but suffer from limited discharge capacities and poor cycling performance.[31] In the third cycle, the CE rises above 97% and steadily improves up to 99.5% which means that SEI formation is completed early on. The specific capacity observed during the first lithiation exceeds the theoretical value for fully lithiated silicon (3579 mA h g^{-1}) due to the formation of the SEI.[32-34] Starting with the second cycle, no excess capacity is recorded and, hence, the newly formed SEI does not contribute to the measured discharge capacity. The recorded specific lithiation capacity in the second cycle is ~3500 mA h g^{-1}, and it remains at a record high in subsequent cycles (*e.g.* ~3450 mA h g^{-1} in the fifth cycle). In comparison, the TzG/Si/CB@Cu electrode prepared together with carbon black does not perform better than the additive-free electrode (Figure S14). Taking the specific lithiation capacity in the second cycle as a baseline, TzG/Si@Cu retains 81.0% of its specific capacity after 50 cycles (2862 mA h g^{-1}) and 69.1% after 100 cycles (2443 mA h g^{-1}) Conversions of these values to areal and volumetric capacities can be found in Figure S15. The remarkable performance parameters of TzG/Si@Cu anodes stem in parts from the increased Si mass loading enabled by our method of preparation (Supplementary Information Table S2 and S3). For comparison, we prepared two electrodes using conventional binders and CB additive,

PVdF/Si/CB@Cu and PAA/Si/CB@Cu (Figure S16).[21,35] These conventional formulations allow a total Si mass loading of up to 60% without compromising the performance of the electrode, compared to 75% of Si in the TzG/Si@Cu system. Overall, the specific capacity and retention of TzG/Si@Cu anodes exceeds that of the best-performing multi-component systems with and without conductivity-enhancing additives that are reported to date (Table S4).[36-45] We propose a number of optimisations for the preparation of TzG/Si@Cu electrodes that lead to improved performance (Supplementary information Section S2.5, Scheme S2-S4, Figure S17-S23 and Table S5). For example, we were able to increase the TzG/Si mass-loading of the electrode beyond 1 mg cm^{-2} by a two rounds of polymerisation on top of a TzG/Si@Cu electrode in the presence of small quantities of $Cu(OAc)_2$ as an additional source of Cu(II) species (Supplementary Information S1.9, Table S5). The obtained electrodes show a stable cycling performance and comparably high capacities as electrodes obtained in a one-step growth process (Figure S24).

TzG is a thermally stable polymer with a decomposition onset above 400 °C under air.[10] Hence, we tested the performance of the TzG/Si@Cu half-cell after a heat treatment of 80 °C for 6 h, above temperatures experienced by Li-ion batteries in some industrial and military settings. The overall performance of the TzG/Si@Cu half-cell after the thermal-stress test remains at ~3000 mA h g^{-1} in the second cycle comparable to the performance of untreated electrodes. The difference in overall capacity and in capacity retention can be attributed to partial decomposition of $LiPF_6$ during the extended heat treatment (Figure S25). As a proof of concept, we assembled a full cell using TzG/Si@Cu as the anode (Si areal mass-loading of 0.291 mg cm^{-2}, specific capacity 3579 mA h g^{-1}) and the commercially available standard NCM811 as the cathode (areal mass-loading of 6.502 mg cm^{-2}, specific capacity ~170 mA h g^{-1}) (Figure S26). The NCM811 cathode was selected over three commercial options (NCM532, NCM622, and NCA) as the one with the highest specific capacity and most stable cycling

performance. Even though the specific capacities of our anode and the commercial standard NCM811 cathode are mismatched, the full-cell assembly shows an acceptable initial CE of 79% that stabilises at >98% after the fourth cycle. Overall, the full-cell has a capacity of 3234 mA h g^{-1} in the third cycle and a capacity retention of 68.2% over 30 cycles (Figure 3c and 3d, Supplementary information Section S2.5, Figure S27). We believe that full-cell assemblies with better coulombic efficiencies can be achieved using cathodes that (i) match the high capacity of our anode better, and (ii) have similar diffusion kinetics.

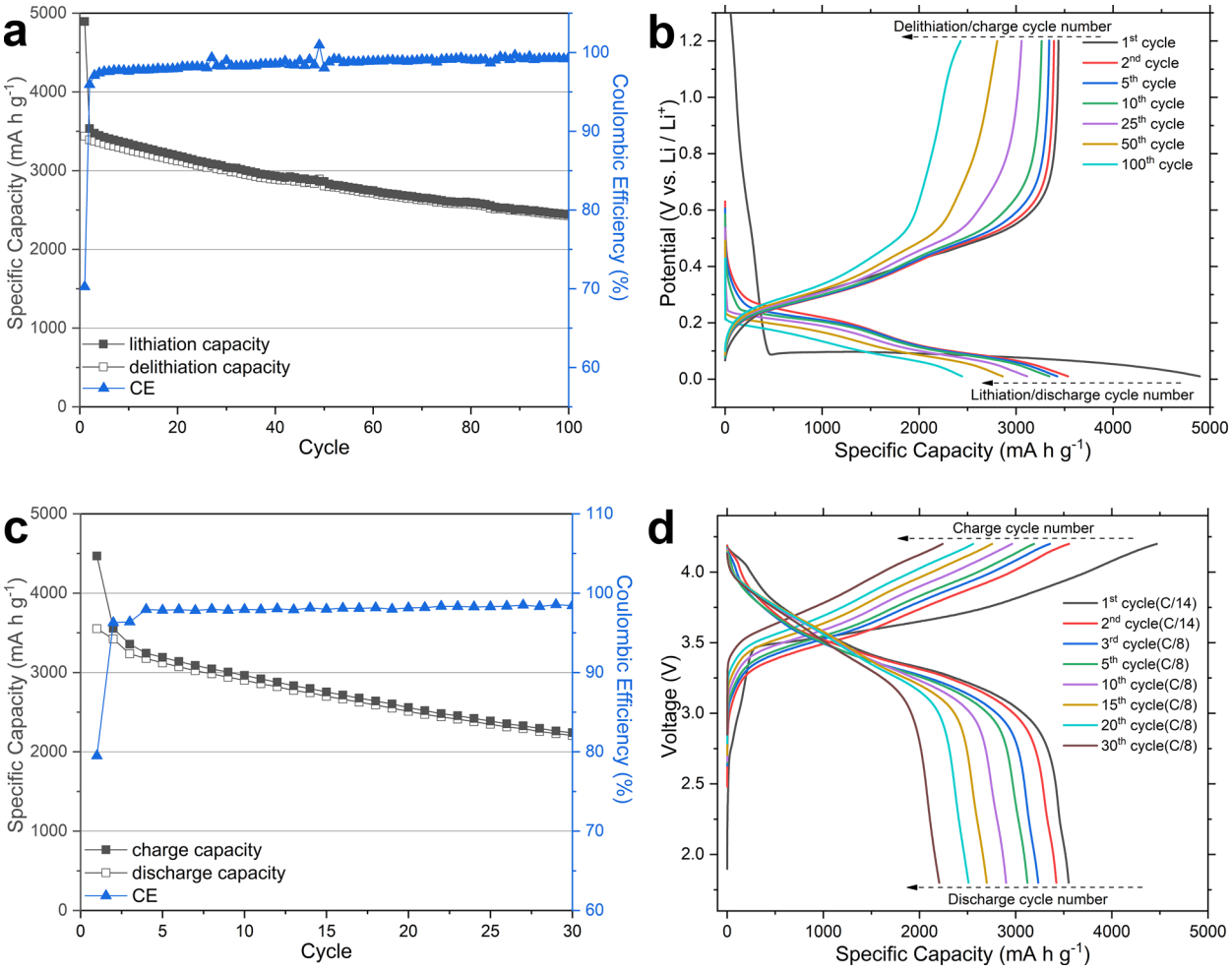

Figure 3. Half-cell performance data of the TzG/Si@Cu electrodes following **method 1**. Galvanostatic charge-discharge cycling with potential limitation (GCPL) uses constant current mode at C/8 within a voltage range of 0.01-1.2 V vs. Li/Li^+. **a**, Specific capacities normalized to Si mass and Coulombic efficiencies (CE) vs. cycle number. **b**, Potential vs. specific capacity curves for consecutive de-/lithiation cycles. Full-cell performance data for an assembly

consisting of a TzG/Si@Cu anode prepared following **method 2** paired with a NCM811 cathode. The n/p ratio is 0.94 (NCM811 loading of 6.502 mg cm^{-1} and Si loading of 0.291 mg cm^{-2}). The full-cell was precycled at C/14 (based on the Si mass-loading) for two initial cycles, and at C/8 for all subsequent cycles, within a potential window of 4.2-1.8 V. **c**, Specific capacities normalized to Si mass / CE vs. cycle number and **d**, charge-discharge curves.

Table 1. Relative molar concentrations of elements as determined by peak integration using X-ray photoelectron spectroscopy (XPS) data recorded at 1486.6 eV for TzG/Si@Cu electrodes at various stages of de-/lithiation cycled at a constant current of 0.32 mA cm^{-2} (i.e. C/8 for the capacity of Si, within 0.01-1.2 V vs. Li/Li^+). (Calculated based on XPS C 1s, Si 2p N 1s, O 1s, Li 1s, F 1s and P 2p spectra).

Sample	Stage during cycling	C (%)	Si (%)	N (%)	O (%)	Li (%)	F (%)	P (%)
TzG/Si@Cu	pristine	17.8	40.8	2.17	39.3	0.00	0.00	0.00
TzG/Si@Cu	1^{st} lithiation	23.0	1.90	0.65	28.2	28.1	15.8	2.36
TzG/Si@Cu	1^{st} delithiation	29.4	1.71	0.16	27.3	22.4	17.8	1.24
TzG/Si@Cu	100^{th} delithiation	44.5	0.84	0.00	32.0	15.9	6.31	0.44

CONCLUSIONS

We present here a one-pot synthetic protocol that yields high-performance silicon-lithium anodes within one hour of reaction time. These anodes consist of silicon nanoparticles that are fully encapsulated by a semi-conducting, porous triazine-based graphdiyne (TzG) polymer that grows directly on the Cu current collector. Cu foil plays three roles in this paradigm-changing

method of anode fabrication: it acts (i) as a source of Cu species for a Glaser-type oxidative coupling polymerization, (ii) as templating substrate for the polymer film, and (iii) as the current collector of the electrode. The porous , semi-conducting TzG polymer acts (i) as a strong, flexible binder that envelops Si NPs with a matrix of covalent bonds that can sustain the dramatic volume changes of silicon in repeated de-/lithiation cycles and prevents detrimental abrasion and reformation of the solid electrolyte interface, (ii) as a facilitator of charge transport along its π-conjugated polymer backbone, and (iii) as a medium for mass transport of lithium ions and electrolyte through its microporous channels. The resulting anodes achieve stable electrochemical cycling performance and an extraordinarily high capacity close to the theoretical limit of electrochemical storage using silicon. The reported process uses raw materials and methods common in industrial electrode manufacture and can be transferred and scaled up with ease. Half-cell electrode assemblies in the off-state retain key performance parameters even after thermal stress, and full-cell cycling tests using commercial cathodes demonstrate the viability of this technology in commercial applications.

Corresponding Author

*Prof. Dr. Michael J. Bojdys, Institut für Chemie and IRIS Adlershof, Humboldt-Universität zu Berlin, Brook-Taylor-Str. 2, 12489 Berlin, Germany & Department of Chemistry, King's College London, Britannia House Guy's Campus, 7 Trinity Street, London, SE1 1DB, UK. E-mail: m.j.bojdys.02@cantab.net

Data availability

All data generated or analysed during this study are provided as a Source Data file at DOI: 10.5281/zenodo.4639826 (URL: https://zenodo.org/record/4639826).

Acknowledgements

We thank Dr. Martin Dračínský for solid-state NMR measurements, Dr. Petr Formánek for TEM imaging and mapping, Prof. Dr. Jürgen P. Rabe for access to Raman spectroscopy. J.H. thanks Dr. Mathias Trunk for providing monomer materials, Weimiao Wang for Raman spectra discussion and analysis. M.J.B. thanks the European Research Council (ERC) for funding under the Starting Grant Scheme (BEGMAT-678462) and the Proof of Concept Grant Scheme (LiAnMat-957534).

Author contributions

J.H. carried out the synthetic experiments and electrochemical tests of electrodes, analyzed the data, and wrote the paper. A.M. carried out the synthetic experiments and electrochemical tests of electrodes, conducted TEM measurements and wrote the paper. A.U. and P.U. carried out the electrochemical tests and analysis of electrodes, which were assembled using Swagelok cell. R.K. carried out the syntheses of monomer/polymer and helped in electrode preparation *via* method 3. M.E. assisted in the preparation of electrodes and electrochemical tests. P.A. and N.K. carried out XPS measurements and analysis. J.M. carried out the SEM measurements. D.B carried out the conductivity measurements and analysis. N.P. provided additional electrochemical system and access to TEM facility and helped in manuscript revision. M.J.B conceived the project, proposed the optimization strategy of electrodes and wrote the paper.

Conflict of interest

The authors declare no conflict of interest.

REFERENCES

1 Schmuch, R., Wagner, R., Hörpel, G., Placke, T. & Winter, M. Performance and cost of materials for lithium-based rechargeable automotive batteries. *Nature Energy* **3**, 267 (2018).

2 Xu, J. *et al.* Recent progress in graphite intercalation compounds for rechargeable metal (Li, Na, K, Al) ‐ ion batteries. *Advanced Science* **4**, 1700146 (2017).

3 Kwon, T.-w., Choi, J. W. & Coskun, A. The emerging era of supramolecular polymeric binders in silicon anodes. *Chemical Society Reviews* **47**, 2145-2164 (2018).
4 Eshetu, G. G. & Figgemeier, E. Confronting the Challenges of Next‐Generation Silicon Anode‐Based Lithium‐Ion Batteries: Role of Designer Electrolyte Additives and Polymeric Binders. *ChemSusChem* **12**, 2515-2539 (2019).
5 Cao, P., Pan, Y., Gao, S., Sun, F. & Yang, H. Polymer Binders Constructed via Dynamic Non‐covalent Bonds for High‐capacity Silicon‐based Anodes. *Chemistry‐A European Journal* (2019).
6 Li, P. *et al.* Recent progress on silicon-based anode materials for practical lithium-ion battery applications. *Energy Storage Materials* **15**, 422-446 (2018).
7 Feng, K. *et al.* Silicon‐Based Anodes for Lithium‐Ion Batteries: From Fundamentals to Practical Applications. *Small* **14**, 1702737 (2018).
8 Liu, N. *et al.* A yolk-shell design for stabilized and scalable Li-ion battery alloy anodes. *Nano Letters* **12**, 3315-3321 (2012).
9 Nguyen, H. T. *et al.* Alumina-coated silicon-based nanowire arrays for high quality Li-ion battery anodes. *Journal of Materials Chemistry* **22**, 24618-24626 (2012).
10 Schwarz, D. *et al.* Twinned Growth of Metal‐Free, Triazine‐Based Photocatalyst Films as Mixed‐Dimensional (2D/3D) van der Waals Heterostructures. *Advanced Materials* **29**, 1703399 (2017).
11 Möhwald, H., Bliznyuk, V. & Kirstein, S. Structure, energy and charge transport in two-dimensional crystals of cyanine dyes. *Synthetic Metals* **61**, 91-96 (1993).
12 Li, Y., Xu, L., Liu, H. & Li, Y. Graphdiyne and graphyne: from theoretical predictions to practical construction. *Chemical Society Reviews* **43**, 2572-2586 (2014).
13 Vyas, V. S. *et al.* A tunable azine covalent organic framework platform for visible light-induced hydrogen generation. *Nature Communications* **6**, 1-9 (2015).
14 Uhlig, F. & Marsmann, H. C. 29Si NMR some practical aspects. *Gelest Catalog*, 208-222 (2008).
15 Park, C.-M. *et al.* Characterizations and electrochemical behaviors of disproportionated SiO and its composite for rechargeable Li-ion batteries. *Journal of Materials Chemistry* **20**, 4854-4860 (2010).
16 Mijatovic, J., Binder, W. H. & Gruber, H. Characterization of surface modified silica nanoparticles by 29 Si solid state NMR spectroscopy. *Microchimica Acta* **133**, 175-181 (2000).
17 Larkin, P., Makowski, M. & Colthup, N. The form of the normal modes of s-triazine: infrared and Raman spectral analysis and ab initio force field calculations. *Spectrochimica Acta Part A: Molecular and Biomolecular Spectroscopy* **55**, 1011-1020 (1999).
18 Li, H. *et al.* The crystal structural evolution of nano-Si anode caused by lithium insertion and extraction at room temperature. *Solid State Ionics* **135**, 181-191 (2000).
19 Philippe, B. *et al.* Role of the LiPF6 salt for the long-term stability of silicon electrodes in Li-ion batteries–A photoelectron spectroscopy study. *Chemistry of Materials* **25**, 394-404 (2013).
20 Radvanyi, E., De Vito, E., Porcher, W. & Larbi, S. J. S. An XPS/AES comparative study of the surface behaviour of nano-silicon anodes for Li-ion batteries. *Journal of Analytical Atomic Spectrometry* **29**, 1120-1131 (2014).
21 Nguyen, C. C., Yoon, T., Seo, D. M., Guduru, P. & Lucht, B. L. Systematic investigation of binders for silicon anodes: interactions of binder with silicon particles and electrolytes and effects of binders on solid electrolyte interphase formation. *ACS Applied Materials & Interfaces* **8**, 12211-12220 (2016).

22 Ferraresi, G., Czornomaz, L., Villevieille, C., Novák, P. & El Kazzi, M. Elucidating the surface reactions of an amorphous Si thin film as a model electrode for Li-ion batteries. *ACS Applied Materials & Interfaces* **8**, 29791-29798 (2016).
23 Schwarz, D. *et al.* Tuning the porosity and photocatalytic performance of triazine‐based graphdiyne polymers through polymorphism. *ChemSusChem* **12**, 194-199 (2019).
24 Xu, J. lnvestigation of the Critical Role of Polymeric Binders for Silicon Negative Electrodes in Lithium-lon Batteries. (2016).
25 Koo, B. *et al.* A highly cross‐linked polymeric binder for high‐performance silicon negative electrodes in lithium ion batteries. *Angewandte Chemie International Edition* **51**, 8762-8767 (2012).
26 Putri, L. K. *et al.* Engineering nanoscale p–n junction via the synergetic dual-doping of p-type boron-doped graphene hybridized with n-type oxygen-doped carbon nitride for enhanced photocatalytic hydrogen evolution. *Journal of Materials Chemistry A* **6**, 3181-3194 (2018).
27 Sakaushi, K. *et al.* An energy storage principle using bipolar porous polymeric frameworks. *Angewandte Chemie International Edition* **51**, 7850-7854 (2012).
28 Sezen, H. & Suzer, S. Communication: Enhancement of dopant dependent x-ray photoelectron spectroscopy peak shifts of Si by surface photovoltage. *The Journal of Chemical Physics* **14**, 141102 (2011).
29 Wertheim, G., Van Attekum, P. T. M. & Basu, S. Electronic structure of lithium graphite. *Solid State Communications* **33**, 1127-1130 (1980).
30 Andersson, A. M., Henningson, A., Siegbahn, H., Jansson, U. & Edström, K. Electrochemically lithiated graphite characterised by photoelectron spectroscopy. *Journal of Power Sources* **119**, 522-527 (2003).
31 Ren, W.-F. *et al.* Improving the Electrochemical Property of Silicon Anodes through Hydrogen-Bonding Cross-Linked Thiourea-Based Polymeric Binders. *ACS Applied Materials & Interfaces* (2020).
32 Obrovac, M. & Christensen, L. Structural changes in silicon anodes during lithium insertion/extraction. *Electrochemical and Solid-State Letters* **7**, A93-A96 (2004).
33 Kovalenko, I. *et al.* A major constituent of brown algae for use in high-capacity Li-ion batteries. *Science* **334**, 75-79 (2011).
34 Urbanski, A. *et al.* An Efficient Two-Polymer Binder for High-Performance Silicon Nanoparticle-Based Lithium-Ion Batteries: A Systematic Case Study with Commercial Polyacrylic Acid and Polyvinyl Butyral Polymers. *Journal of The Electrochemical Society* **166**, A5275-A5286 (2019).
35 Karkar, Z., Guyomard, D., Roué, L. & Lestriez, B. A comparative study of polyacrylic acid (PAA) and carboxymethyl cellulose (CMC) binders for Si-based electrodes. *Electrochimica Acta* **258**, 453-466 (2017).
36 Chen, Z. *et al.* High‐areal‐capacity silicon electrodes with low‐cost silicon particles based on spatial control of self‐healing binder. *Advanced Energy Materials* **5**, 1401826 (2015).
37 Choi, S., Kwon, T.-w., Coskun, A. & Choi, J. W. Highly elastic binders integrating polyrotaxanes for silicon microparticle anodes in lithium ion batteries. *Science* **357**, 279-283 (2017).
38 Higgins, T. M. *et al.* A commercial conducting polymer as both binder and conductive additive for silicon nanoparticle-based lithium-ion battery negative Electrodes. *ACS Nano* **10**, 3702-3713 (2016).

39 Jeong, Y. K. *et al.* Millipede-inspired structural design principle for high performance polysaccharide binders in silicon anodes. *Energy & Environmental Science* **8**, 1224-1230 (2015).
40 Liu, G. *et al.* Polymers with tailored electronic structure for high capacity lithium battery electrodes. *Advanced Materials* **23**, 4679-4683 (2011).
41 Song, J. *et al.* Interpenetrated gel polymer binder for high‐performance silicon anodes in lithium‐ion batteries. *Advanced Functional Materials* **24**, 5904-5910 (2014).
42 Wang, C. *et al.* Self-healing chemistry enables the stable operation of silicon microparticle anodes for high-energy lithium-ion batteries. *Nature Chemistry* **5**, 1042 (2013).
43 Wu, H. *et al.* Stable Li-ion battery anodes by in-situ polymerization of conducting hydrogel to conformally coat silicon nanoparticles. *Nature Communications* **4**, 1943 (2013).
44 Zeng, W. *et al.* Enhanced Ion Conductivity in Conducting Polymer Binder for High‐Performance Silicon Anodes in Advanced Lithium‐Ion Batteries. *Advanced Energy Materials* **8**, 1702314 (2018).
45 Zhang, G. *et al.* A Quadruple‐Hydrogen‐Bonded Supramolecular Binder for High‐Performance Silicon Anodes in Lithium‐Ion Batteries. *Small* **14**, 1801189 (2018).